Video Article

Visually Based Characterization of the Incipient Particle Motion in Regular Substrates: From Laminar to Turbulent Conditions

José R. Agudo[1], Jiwon Han[1], Jinyoung Park[1], Sinyoung Kwon[1], Soebiakto Loekman[2], Giovanni Luzi[1], Christoph Linderberger[3], Antonio Delgado[1,4], Andreas Wierschem[4]

[1]Institute of Fluid Mechanics, FAU Busan Campus, University of Erlangen-Nuremberg

[2]Institute of Chemical Reaction Engineering, FAU Busan Campus, University of Erlangen-Nuremberg

[3]Institute of Bioprocess Engineering, FAU Busan Campus, University of Erlangen-Nuremberg

[4]Institute of Fluid Mechanics, Friedrich-Alexander-Universität Erlangen-Nürnberg (FAU)

Correspondence to: José R. Agudo at jaratg@gmail.com

URL: https://www.jove.com/video/57238
DOI: doi:10.3791/57238

Keywords: Engineering, Issue 132, Granular Flow, Particle/Fluid Flow, Sediment Transport, Incipient Motion

Date Published: 2/22/2018

Citation: Agudo, J.R., Han, J., Park, J., Kwon, S., Loekman, S., Luzi, G., Linderberger, C., Delgado, A., Wierschem, A. Visually Based Characterization of the Incipient Particle Motion in Regular Substrates: From Laminar to Turbulent Conditions. *J. Vis. Exp.* (132), e57238, doi:10.3791/57238 (2018).

Abstract

Two different experimental methods for determining the threshold of particle motion as a function of geometrical properties of the bed from laminar to turbulent flow conditions are presented. For that purpose, the incipient motion of a single bead is studied on regular substrates that consist of a monolayer of fixed spheres of uniform size that are regularly arranged in triangular and quadratic symmetries. The threshold is characterized by the critical Shields number. The criterion for the onset of motion is defined as the displacement from the original equilibrium position to the neighboring one. The displacement and the mode of motion are identified with an imaging system. The laminar flow is induced using a rotational rheometer with a parallel disk configuration. The shear Reynolds number remains below 1. The turbulent flow is induced in a low-speed wind tunnel with open jet test section. The air velocity is regulated with a frequency converter on the blower fan. The velocity profile is measured with a hot wire probe connected to a hot film anemometer. The shear Reynolds number ranges between 40 and 150. The logarithmic velocity law and the modified wall law presented by Rotta are used to infer the shear velocity from the experimental data. The latter is of special interest when the mobile bead is partially exposed to the turbulent flow in the so-called hydraulically transitional flow regime. The shear stress is estimated at onset of motion. Some illustrative results showing the strong impact of the angle of repose, and the exposure of the bead to shear flow are represented in both regimes.

Video Link

The video component of this article can be found at https://www.jove.com/video/57238/

Introduction

Incipient particle motion is encountered in a wide range of industrial and natural processes. Environmental examples include the initial process of sediment transport in river and oceans, bed erosion or dune formation among others [1,2,3]. Pneumatic conveying[4], removal of pollutants or cleaning of surfaces[5,6] are typical industrial applications involving the onset of particle motion.

Due to the broad range of applications, the onset of particle motion has been extensively studied over a century, mostly under turbulent conditions[7,8,9,10,11,12,13,14,15]. Many experimental approaches have been applied to determine the threshold for the onset of motion. The studies include parameters such as the particle Reynolds number[13,16,17,18,19,20], the relative flow submergence[21,22,23,24] or geometrical factors as the angle of repose[16,18,25], exposure to the flow[26,27,28,29], relative grain protrusion[29] or streamwise bed slope[30].

The current data for the threshold including turbulent conditions are broadly scattered[12,31] and the results often seem inconsistent[24]. This is mostly due to the inherent complexity of controlling or determining flow parameters under turbulent conditions[13,14]. Besides, the threshold for sediment motion strongly depends on the mode of motion, *i.e.* sliding, rolling or lifting[17] and the criterion to characterize the incipient motion[31]. The latter may be ambiguous in an erodible sediment bed.

During the last decade, experimental researchers have studied incipient particle motion in laminar flows[32,33,34,35,36,37,38,39,40,41,42,43,44], where the wide spectrum of length scales interacting with the bed is avoided[45]. In many practical scenarios implying sedimentation, the particles are quite small and the particle Reynolds number remains lower than about 5[46]. On the other hand, laminar flows are able to generate geometric patterns as ripples and dunes as turbulent flows do[42,47]. Similitudes in both regimens have been shown to reflect analogies in the underlying physics[47] so important insight for the particle transport can be obtained from a better controlled experimental system[48].

In laminar flow, Charru *et al.* noticed that the local rearrangement of a granular bed of uniformly sized beads, so-called bed armouring, resulted in a progressive increase of the threshold for the onset of motion until saturated conditions were achieved[32]. Literature, however, reveals different

thresholds for saturated conditions in irregularly arranged sediment beds depending on the experimental set-up[36,44]. This scattering may be due to the difficulty of controlling particle parameters such as orientation, protrusion level and compactness of the sediments.

The main goal of this manuscript is to describe in detail how to characterize the incipient motion of single spheres as a function of geometrical properties of the horizontal sediment bed. For that purpose, we use regular geometries, consisting of monolayers of fixed beads regularly arranged according to triangular or quadratic configurations. Regular substrates similar to that we use are found in applications such as for the template-assembly of particles in microfluidic assays[49], self-assembly of microdevices in confined structured geometries[50] or intrinsic particle-induced transport in microchannels[51]. More importantly, using regular substrates allows us to highlight the impact of local geometry and orientation and to avoid any dubiety about the role of the neighborhood.

In laminar flow, we observed that the critical Shields number increased by 50% only depending on the spacing between the substrate spheres and thus on the exposure of the bead to the flow[38]. Similarly, we found that the critical Shields number changed by up to a factor of two depending on the orientation of the substrate to the flow direction[38]. We noticed that immobile neighbors only affect the onset of the mobile bead if they were closer than about three particle diameters[41]. Triggered by the experiment findings, we have recently presented a rigorous analytical model that predicts the critical Shields number in the creeping flow limit[40]. The model covers the onset of motion from highly exposed to hidden beads.

The first part of this manuscript deals with the description of the experimental procedure used in previous studies at shear Reynolds number, Re*, lower than 1. The laminar flow is induced with a rotational rheometer with a parallel configuration. In this low Reynolds number limit, the particle is not supposed to experience any velocity fluctuation[20] and the system matches the so-called hydraulically smooth flow where the particle is submerged within the viscous sublayer.

Once incipient motion at laminar flow is established, the role of turbulence can become clearer. Motivated by this idea, we introduce a novel experimental procedure in the second part of the protocol. Using a Göttingen low-speed wind tunnel with open jet test section, the critical Shields number can be determined in a wide range of Re* including the hydraulically transitional flow and the turbulent regime. The experimental results can provide important insight about how forces and torques act on a particle due to the turbulent flow depending on the substrate geometry. Besides, these results can be used as a benchmark for more sophisticated models at high Re* in a similar way that past work in laminar flow has been used to feed semi probabilistic models[52] or to validate recent numerical models[53]. We present some representative examples of applications at Re* ranging from 40 to 150.

The incipient criterion is established as the motion of the single particle from its initial equilibrium position to the next one. Image processing is used to determine the mode of onset of motion, *i.e.* rolling, sliding, lifting[39,41]. For that purpose, the angle of rotation of mobile spheres that were manually marked is detected. The algorithm tracks the position of the marks and compares it with the center of the sphere. A preliminary set of experiments was conducted in both experimental set-ups to clarify that the critical Shields number remains independent of finite size effects of the set-up and relative flow submergence. The experimental methods are thus designed to exclude any other parameter dependent on the critical Shields number beyond Re* and geometrical properties of the sediment bed. The Re* is varied using different fluid-particle combinations. The critical Shields number is characterized as a function of the burial degree, ζ, defined by Martino *et al.*[37] as $\tan\varphi / E$ where φ is the angle of repose, *i.e.* the critical angle at which motion occurs[54], and E is the exposure degree, defined as the ratio between the cross-sectional area effectively exposed to the flow to the total cross-sectional area of the mobile bead.

Protocol

1. Incipient Particle Motion in the Creeping Flow Limit.

NOTE: The measurements are conducted in a rotational rheometer that has been modified for this specific application.

1. **Preparing the Rheometer.**
    1. Connect the air supply to the rheometer in order to avoid damaging the air bearings. Open the valve besides the air filters until a pressure of approximately 5 bars in the system is achieved.
    2. Connect the fluid circulator to the measuring plate. Ensure that the hoses of the Peltier element are connected to the rheometer. Switch on the fluid circulator and set the desired temperature (20 °C).
    3. Mount the customized container containing the regular substrate on the rheometer.
        1. Take the regular substrate out of the container and clean the surface carefully with distilled water. Dry the surface with a lens cleaning cloth and remove possible residual dust with a blower.
        NOTE: The regular substrates are monolayers of 15 x 15 mm^2 built from spherical soda-lime glass beads of (405.9 ± 8.7) µm.
        2. Using 0.4 mm thickness double-sided tape, fix the regular substrate into the container ensuring that the substrate center is at a distance of 21 mm from the turning axis.
        3. Place the customized adapter on the rheometer plate.
        4. Mount the customized circular container into the plate ensuring that the flat front section is facing the imaging system designed for side recording.
        NOTE: Ensure that the container is completely horizontal with the water level (0.6 mm/m). For that purpose, place the water level on the container parallel to the back of the device and level it with the rheometer adjustable feet. Repeat the procedure turning the water level by 90 degrees.
    4. Switch on the rheometer. Wait until the boot procedure is finished and the status "ok" appears on the device screen.
    5. Start the computer and the rheometer software. Initialize the rheometer and set the temperature control from the control panel of the software to the desired value (20 °C).
    6. Mount the customized measuring system. Set-up the zero gap from the software.

NOTE: Before setting the zero gap, ensure that there are no mobile beads on the substrate and that the substrate borders are not bent. An error in setting the zero-gap will lead to a systematic error in the calculation of the shear rate and therefore in the subsequent measurement of the critical Shields number. An absolute uncertainty of 0.05 mm is assumed in the gap width when calculating the critical Shields number.

7. Lift the measuring plate to 30 mm and remove it.
8. Fill the container with approximately 70 mL of 100 mPa·s silicon oil. Ensure that the level of the fluid in the container remains above 2 mm. The silicon oil should not cover the upper part of the transparent plate. Wait approximately 15-20 min for the thermal equilibrium. During that time, adjust the imaging systems (see step 2 from the protocol).
NOTE: The temperature that is fixed to (295.15 ± 0.5) K here, is controlled with a Peltier element connected to the rheometer and measured with an external thermometer. Fluctuations of less than 0.5 K are observed during the experiments.

2. **Adjusting the imaging system.**
   1. Switch on the 300 W Arc Xenon Lamp. Adjust the flexible light guide to illuminate the bead from the side through the transparent walls of the container.
   2. Adjust the LED light intensity to avoid strong light reflection on the substrate.
   3. Adjust the imaging system designed for recording the particle motion from the top through the transparent measuring plate.
      1. Start-up the imaging software from the computer and choose the monochrome profile from the start dialog.
      2. Open the 768 x 576 CMOS camera of the imaging system installed on the top of the container. Start up the live video.
      3. Adjust the horizontal positioning stage until the reference position that has been previously marked in the center of the substrate appears in the center of the image.
      4. Adjust the vertical positioning stage to focus on the substrate.
      5. Place carefully a marked soda-lime glass sphere of (405.9 ± 8.7) µm.
      6. Ensure that at least one of the marks is placed at a distance of approximately 75% of the bead radius or larger from the axis of rotation. If this is not the case, move manually the measuring plate to achieve the motion of the bead to the next equilibrium position (see **Figure 2(a)** as a reference).
      NOTE: To ensure proper monitoring during motion the mobile beads are marked with several spots separated by about 45° (see **Figure 3(a)**). The code includes a simple control flow statement to minimize mark misassignment in order to calculate the angle of rotation. For further details, we refer to Agudo *et al.* 2017[39].
      7. Open the dialog box for setting the camera parameters and adjust the frame rate to 30 fps. Adjust the exposure time to ensure that the marks are properly distinguished from the bead perimeter.
      NOTE: The soda-lime glass sphere submerged into a silicon oil of 100 mPa·s requires about 4 seconds to move from its initial position to the watershed to the neighboring equilibrium position. Hence, a framerate of 30 fps permits an uncertainty of less than 1%.

   4. Mount the measuring plate to the rheometer.
   5. Set the measuring distance to 2 mm.
   NOTE: The focus of the top camera must be slightly readjusted due to the presence of the Plexiglas plate.
   6. Adjust the imaging system designed for recording the particle motion from the side through the transparent microscope slide.
      1. Open the 4912 x 3684 CMOS camera of the imaging system installed at the front of the container and start up the live video.
      2. Adjust the vertical and the horizontal positioning stage placed parallel to the rheometer until the marked bead appears in the center of the image.
      3. Adjust the modular zoom lens until the field of view includes the upper surface of the substrate, the bead, and the bottom part of the measuring disk.
      4. Adjust the horizontal positioning stage placed perpendicular to the rheometer to focus on the bead.
      5. Open the dialog box for setting the camera parameters and adjust the frame rate to 30 fps.

3. **Determine the critical rotating speed for the onset of motion.**
   1. Increase linearly the rotational speed, n, from 0.02 to 0.05 revolutions per second in small increments of 0.00025 revolutions per second using the rheometer software.
      1. In the measurement window, double-click the cell for the control type and edit the range of the speed from 0.02 to 0.05 revolutions per second.
      2. Double-click the time setting and enter the number of measurement points, 60, and the duration of each measurement, 5 s.
      3. Set a table representing the rotational speed as a function of time.

   2. Open the live video from the top and side cameras. Start recording a video-sequence from both cameras using the imaging software.
   3. Start the measurement using the rheometer software.
   NOTE: A preliminary experiment with a larger step size is recommended prior to step 1.3.1.1 in order to roughly estimate the speed range at which the incipient motion will happen. At a distance of 21 mm from the turning axis and using the silicone oil of 100 mPa·s, for instance, the glass bead moves at rotating speeds of approximately 0.035 revolutions per second. Hence, a range from 0.02 to 0.05 revolutions per second seems appropriate for the experiment.
   4. Look carefully at the live video from the top or from the side camera and stop the measurement when the bead displaces from its equilibrium position. Note the speed at which the bead crosses the separatrix to the neighboring equilibrium position. The noted rotating speed represents the critical rotating speed, n_C. Stop the video-sequences.
   NOTE: Ensure that the step size is small enough that the increase of speed during the time interval that the bead requires moving from its initial position to the neighboring one does not involve more than 1% of the critical value.
   5. Place the bead back to its original position. This can be done by moving manually the rotating plate until the bead displaces one position back. Repeat the experiment five times noting the mean critical speed and the standard deviation.
   6. Repeat the steps 1.3.1 to 1.3.5 with a different marked bead in 2 adjacent positions to the center of the substrate.

4. **Analyzing the data.**

1. Determine the mode of motion: analyze the sequence of images previously recorded from the top or from the side with the algorithm as described in Agudo *et al.* 2017[39].
2. Determine the critical Shields number and the shear Reynolds number.
   1. Obtain the critical Shields number from the following equation[40]

$$\theta_C = \frac{2\pi\nu r}{\left(\frac{\rho_P}{\rho} - 1\right) hgD_P} n_C \qquad (1)$$

   where n_C has been obtained from step 1.3.4, $\nu = \mu / \rho$ is the kinematic viscosity, ρ_P and ρ are particle and liquid densities, respectively, g is the acceleration of gravity and D_P is the mobile bead diameter, all of them known. h is the gap width, defined as the distance from the top of the substrate spheres to the measuring plate, *i.e.* 2 mm and *r* is the radial distance of the particle from the turning axis, *i.e.* 21 mm.
   2. Obtain the shear Reynolds number, Re* based on the shear velocity, from the following equations:

$$\mathrm{Re}^* = \left(\frac{2\pi r}{\nu h} n_C\right)^{0.5} D_P \qquad (2)$$

3. Repeat the procedure from 1.1.3 to 1.4.2 using a different regular substrate.
4. Use different bead densities and different fluid viscosities in order to cover a broad range of the Re* from creeping flow conditions up to 1.

2. Incipient Particle Motion at the Hydraulically Transitional and Rough Turbulent Regime.

NOTE: The measurements are conducted in a customized low-speed Wind-tunnel with open jet test section, Göttingen type.

1. **Preparing the imaging system.**
   1. Fix the quadratic substrate in the middle of the test section.
   2. Place a 5 mm alumina bead previously marked at the desired initial position (110 mm from the leading edge and 95 mm from the side edge).
   3. Connect the high-speed camera coupled to the macro lens to the computer and switch it on. Adjust the macro lens until the target bead is clear in the image.
   4. Initiate the imaging software on the computer. Activate "Live Camera", and set the "Sample rate" to 1000 fps.
   5. Switch on the LED light source and adjust the intensity as well as the focus of the camera to achieve a clear image of the particle and its marks.
      NOTE: Ensure that at least one of the marks is placed at a distance of approximately 75% of the bead radius or larger from the axis of rotation (see **Figure 3(a)** as a reference).

2. **Determining the critical fan speed for the onset of motion.**
   1. Set the fan speed well below the critical value (approximately 1400 rpm for the 5 mm alumina bead).
   2. Start the recording by pressing the trigger on the imaging software.
   3. Increase the speed in steps of approximately 4 to 6 rpm every 10 s until incipient motion occurs.
   4. Note the critical speed value at which incipient motion occurs and stop the video sequence.
   5. Place a new marked bead at the same initial position and repeat the procedure from 2.2.1 to 2.2.4 ten times. Note the critical speed for each measurement.
   6. Repeat the procedure from 2.2.1 to 2.2.5 at the same distance from the leading edge but at 65 and 125 mm from the side edge, respectively. Note the critical speed for each measurement.

3. **Preparing the constant temperature hot-wire anemometer (CTA).**
   1. Set the CTA control function to stand by and the decade resistance to 00.00. Switch on the main power and wait for approximately 15-20 min to warm up.
   2. Plug the shorting probe and switch the CTA control function to resistance measurement. Adjust the zero Ohms until the needle is placed in the red mark and switch back the control function to standby.
   3. Replace the shorting probe by the miniature hot-wire probe. Switch the CTA control function to resistance measurement. Adjust the resistance switches until the needle is placed in the red mark.
      NOTE: The measured resistance corresponds to the cold resistance of the miniature probe. The measured value should be in agreement with the value provided by the manufacturer (3.32 Ω).
   4. Switch the CTA function to stand by and adjust the resistance decade to 5.5 Ω to achieve an overheat ratio of about 65%.
   5. Measure the frequency response of the CTA at the mean critical speed (step 2.2.4).
      1. Switch on the fan and set the rotational speed of the fan to the critical value, about 1400 rpm. Switch on the oscilloscope.
      2. Switch the square wave generator of the CTA on.

3. Initiate the oscilloscope software on the computer and open the CSV module to enable the data recording. Choose the channel (CH1) and save the recording data i.e. time and voltage, under the desired file name. Wait until the measurements finish (about 3 min).
   NOTE: The cut-off frequency is calculated from the response time at which the voltage dropped to a level of - 3db (see **Figure 4(a)**).
4. Switch the square wave generator off and set the CTA function to standby.

4. **Calibrating the CTA.**
   1. Switch the CTA function to operate. Ensure that the probe is adjusted to a sufficient height away from the plate so that it is located in the free stream zone.
   2. Set the fan rotational speed to 200 rpm. Measure the streamwise velocity in the free stream zone using the impeller anemometer and read the voltage on the oscilloscope.
   3. Repeat step 2.4.2 for different rotational speeds with a fixed increment of 50 rpm up to about 1450 rpm (a total of 26 reads).
   4. Establish a correlation between the rpm and the measured free-stream streamwise velocity, U_∞. Obtain the critical velocity, $U_{\infty,C}$, corresponding to the critical rotational speed for each of the measurements performed from steps 2.2.5 to 2.2.6. Calculate the mean critical free-stream velocity, $\overline{U}_{\infty,C}$ and the standard deviation of the measurements.
   5. Establish a correlation between the velocity and the voltage according to a third-degree polynomial fit:
      $$u = x_1 \cdot E^3 + x_2 \cdot E^2 + x_3 \cdot E + x_4 \quad (3)$$
      Here, u is the streamwise velocity measured in m/s, E is the voltage measured in Volt (V), and x_i are the fit coefficients. The calibration curves are shown in **Figure 4(b)** before and after the measurements of the velocity profile.

5. **Measuring the streamwise velocity with the wall-normal position at critical conditions.**
   1. Remove the marked bead from the substrate.
   2. Adjust the handwheel of the horizontal positioning stage until the hot wire probe is placed at the desired initial position (110 mm from the leading edge and 95 mm from the side edge).
   3. Adjust carefully the handwheel of the vertical positioning stage until the probe is placed as close as possible to the substrate surface. See through the camera coupled to the macro lens to ensure that the wire does not touch the substrate surface. Set the zero value in the digital level indicator at that position.
      Caution: The hot wire is very sensitive and if it touches the surface it will break. For sake of security, we place the probe at a distance of 0.05 mm above the top of the substrate sphere (see **Figure 1(e)** as a reference). This represents a normalized wall-normal component $y_o^+ = \frac{y_0 \cdot u^*}{\nu} \approx 2.6$ where y_0 is the starting measuring value, u^* is the shear velocity and ν is the kinematic viscosity of air at operating temperature. Note that the starting value is below $y_o^+ \approx 5$ where the viscosity is dominant[55].
   4. Set the fan rotational speed to the mean rotational speed at which the incipient motion occurs, see step 2.2.4. The free-stream velocity thus corresponds to $U_{\infty,C}$.
   5. Adjust the sampling rate to 1 kSa and the number of samples to 6000 on the oscilloscope (total sampling time of 6 s). Choose the channel (CH1) and start the measurement. Save the recording data under the desired file name. Wait until the measurements finish (about 3 min).
   6. Increase the wall-normal position of the probe by an increment of 0.01 mm up to 0.4 mm, and by an increment of 0.1 mm up to the height of 10 mm. This corresponds to a total of 137 points for the velocity profile curve. Save the recorded data for each height.

6. **Analyzing the data.**
   1. Calculate the mean streamwise velocity and the turbulent intensity for each wall-normal position.
      1. Run the self-developed algorithm to evaluate the statistical quantities. Open the script and select the folder containing the calibration curve and the stored data for each of the measured height.
         NOTE: The script computes first the fit coefficients from the calibration curve as shown in Eq. 3. For each height, it calculates the instantaneous streamwise velocity, u by using Eq. 3 and computes the integral time scale by the autocorrelation method[56]. Thereafter, it computes the time average, $\overline{u}$ and the root square velocity, u_{rms}, for samples that are separated by two times the integral time necessary for the time-averaged analysis.
      2. Plot the dimensionless vertical position, y/d_P against the dimensionless streamwise time average velocity $\overline{u}/U_{\infty,C}$, where d_P is the diameter of the substrate spheres. Plot y/d_P against the dimensionless root square velocity $u_{rms}/U_{\infty,C}$. **Figure 4(c)-(d)** depicts the results for the case of the 5 mm alumina bead.
   2. Calculate the shear velocity from the experimental data.
      1. Fit the dimensionless time average velocity with the logarithmic velocity distribution[57]

$$\frac{\overline{u}}{u^*} = \frac{1}{\kappa}\ln\left(\frac{y}{d_P}\right) + A \quad (5)$$

where u^* is the shear velocity, κ is the von Kármán's constant and A is a constant that depends on the shear Reynolds number[26]. The solid line in **Figure 4(c)** is a logarithmic fit to the time average velocity.

NOTE: From the fit to the experimental data, it can be shown that the shear velocity, u^* is given by:

$$u^* = \frac{\kappa}{b} U_{\infty,C} \quad (6)$$

where b is the logarithmic fit coefficient and $\kappa = 0.41$[20].

The viscous sublayer, δ_S remains above the top of the substrate spheres in our experiments. In the most rigorous scenario, Eq. 5 should be replaced by the modified velocity law presented by Rotta[20,58].

$$\frac{\overline{u}}{u^*} = \frac{1}{\kappa\xi(y)}\left(0.5 - \sqrt{\xi^2(y) + 0.25}\right) + \frac{1}{\kappa}\ln\left(2\xi(y) + 2\sqrt{\xi^2(y) + 0.25}\right) + \mathrm{Re}_\nu \quad (7)$$

where $\xi(y) = \kappa \mathrm{Re}^* \left(y - \delta_S\right) / d_P$ and $\mathrm{Re}_\upsilon = u^* \delta_S / \upsilon$. δ_S is the viscous sublayer thickness that can be approximately calculated by $\delta_S = 5 \cdot \upsilon / u^*$[55].

The algorithm computes directly the shear velocity from the fit of experimental data to Eq. 5 and Eq. 7. The blue symbols in **Figure 4**(c) represent the fit to the experimental data according to Eq. 7.

At Re* above 70, δ_S represents up to 5% of the mobile bead diameter, and using a fit from Eq. 5 or Eq. 7 involves a variation on u^* within the adopted range of uncertainty. Compare solid line and blue symbols in **Figure 4**(c) at a Re* of about 87.5.

3. Determine the mode of motion: analyze the sequence of images previously recorded from the side with the algorithm as described in Agudo *et al.* 2017[39].
4. Determine the critical Shields number and the shear Reynolds number.
    1. Obtain the critical Shields number from the following equation[22]

$$\theta_C = \frac{\left(u^*\right)^2}{\left(\frac{\rho_P}{\rho} - 1\right) g D_P} \quad (8)$$

where u^* has been obtained from step 10.2, ρ_P and ρ are particle and fluid densities, respectively, g is the acceleration of gravity and D_P is the mobile bead diameter, all of them known.

    2. Obtain the particle Reynolds number, Re*, from the following equations:

$$\mathrm{Re}^* = \frac{u^* d_P}{\nu} \quad (9)$$

    3. Repeat the procedure for measuring the velocity profile as a function of the wall-normal coordinate, step 2.5, at the same distance from the leading edge but at 65 and 125 mm in the width direction, respectively.
    4. Repeat the procedure from 2.1 to 2.6.4.3 using different bead sizes and regular substrates.

Representative Results

Figure 1(a) represents a sketch of the experimental set-up used to characterize the critical Shields number in the creeping flow limit, Section 1 of the protocol. The measurements are conducted in a rotational rheometer that was modified for this specific application. A transparent Plexiglas plate of 70 mm in diameter was carefully fixed to a parallel plate of 25 mm in diameter. The inertia of the measuring system was therefore readjusted before the measurement. A customized circular container of 176 mm in diameter with transparent walls was concentrically coupled to the rheometer. A vertical cut was performed in the front section. A microscope slide was carefully fixed to the front section to improve the imaging. The gap setting profile was readjusted to take into account the presence of the container. The plate velocity was minimized close to the fluid interface to avoid the bead movement before starting the measurement. In that system, the single bead can be optically tracked from the top through the transparent plate, see **Figure 1(b)**, or from the side through the transparent sidewalls, see **Figure 1(c)**. A Couette flow profile is induced between the rotating plate and the substrate. Therefore, the critical shear rate is given by $\dot{\gamma}_c = 2\pi r n_c / h$. Accordingly, the critical Shields number and the shear Reynolds number can be defined as in Eq. 1 and Eq. 2, respectively. The set-up used in Section 2 of the protocol is illustrated in **Figure 1(d)**. The measurements are conducted in a customized low-speed Wind-tunnel with open jet test section, Göttingen type. The regular substrates of 19 x 25 cm^2 are located in the middle of the test section. The fan speed and thus the fluid velocity is regulated with a frequency converter connected to the blower fan. A turbulent boundary layer is induced above the regular substrate. The velocity profile is measured with a hot wire miniature probe specialized designed for measuring the boundary layer (see **Figure 1(e)**) coupled to a constant temperature anemometer (CTA). The wall-normal position, *y*, is controlled with a vertical stage that can be repositioned within approx. 0.01 mm. The position is measured with a digital level indicator with a resolution of 0.01 mm. In the fully rough turbulent regime (typically Re*>70), the shear velocity can be inferred from a fit of the experimental data to the logarithmic wall law, Eq. 5[59]. In the hydraulically transition regime, the shear velocity is inferred from a fit to the modified wall law, Eq. 7[58]. The critical Shields number and the shear Reynolds number can be obtained from the shear velocity as expressed in Eq. 8 and Eq. 9, respectively.

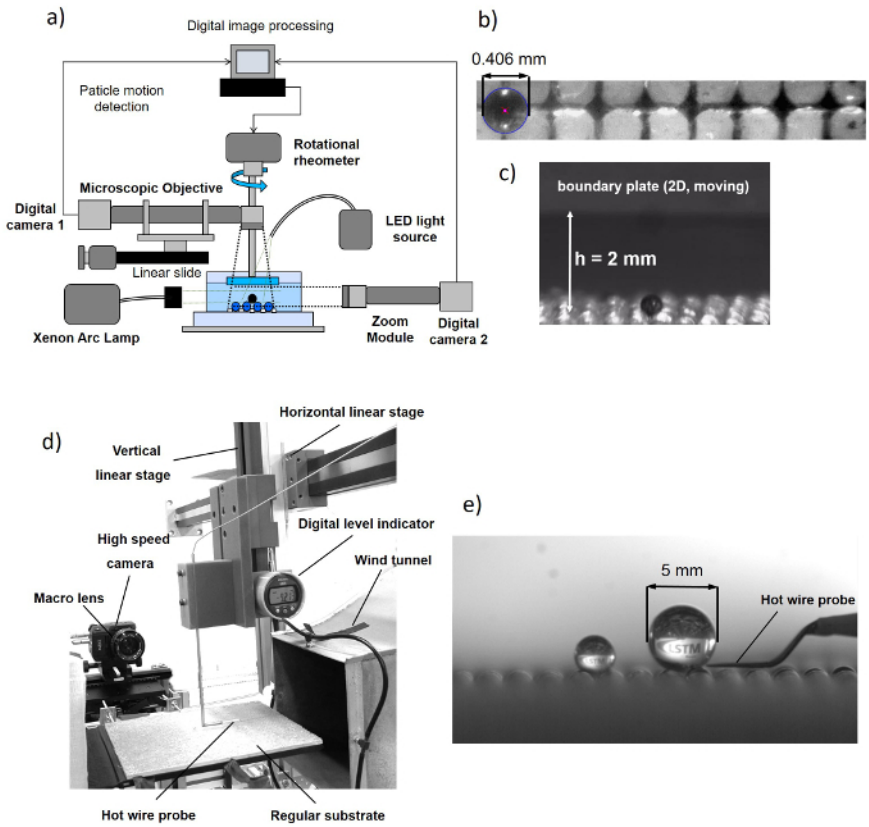

Figure 1: Sketch of the experimental set-up used at laminar conditions (a). A mobile bead of (405.9 ± 8.7) µm diameter resting on the quadratic substrate made of spheres of same size with a spacing of 14 µm between them viewed from the top (b) and from the side (c), respectively. Sketch of the experimental set-up used at turbulent conditions (d). Two mobile beads of (3.00 ± 0.15) mm and (5.00 ± 0.25) mm resting on a quadratic substrate with no spacing between spheres of (2.00 ± 0.10) mm close to the miniature hot-wire probe (e). The probe is placed at a distance of approximately 0.05 mm from the top of the substrate sphere. **Figure 1(d)** is reproduced from Agudo *et al.* 2017a[39], with the permission of AIP Publishing. Please click here to view a larger version of this figure.

An image process routine that analyzes marked beads was developed in previous studies[39] to calculate the angle of rotation of the bead at onset of motion. **Figure 2** and **Figure 3** depict examples of applicability at laminar, Re* = 0.06, and turbulent conditions, Re* = 87.5, respectively. Using marked spheres, we obtained the same critical Shields number as for beads without marks within measurement uncertainty. Based on Canny edge detection and Hough transform, the routine is able to recognize the bead with relative uncertainties ranging between 1.2 and 4%[39]. The rotation angle is determined by tracking marks based on a gray-scale thresholding. The uncertainty, in this case, increases up to absolute values ranging from 7° to 17°, depending on the imaging system[39]. Snapshots in **Figure 2(a) - (f)** illustrate representative examples for the single glass bead of (405.9 ± 8.7) µm displacing from its initial equilibrium position to the next one on a quadratic substrate made of beads of same size with a gap of 14 µm between spheres. The video has been recorded from the top through the transparent measuring system as described in Section 1 (see step 1.2.3). **Figure 2(g)** shows the angle of rotation during the displacement as a function of the curved trajectory ΔL along the substrate (see inset of **Figure 2(g)**). The trajectory is normalized to the distance traveled by the bead along the curved path between two equilibrium positions, L. The dotted line in **Figure 2(g)** represents the angle for pure rolling. The single bead experiences a total rotation of (140 ± 8.5)° which coincides with the angle for pure rolling motion, which also has a value of approximately 140°. Rolling is thus the mode of incipient motion and Eq. 1 can be used to characterize the incipient particle motion.

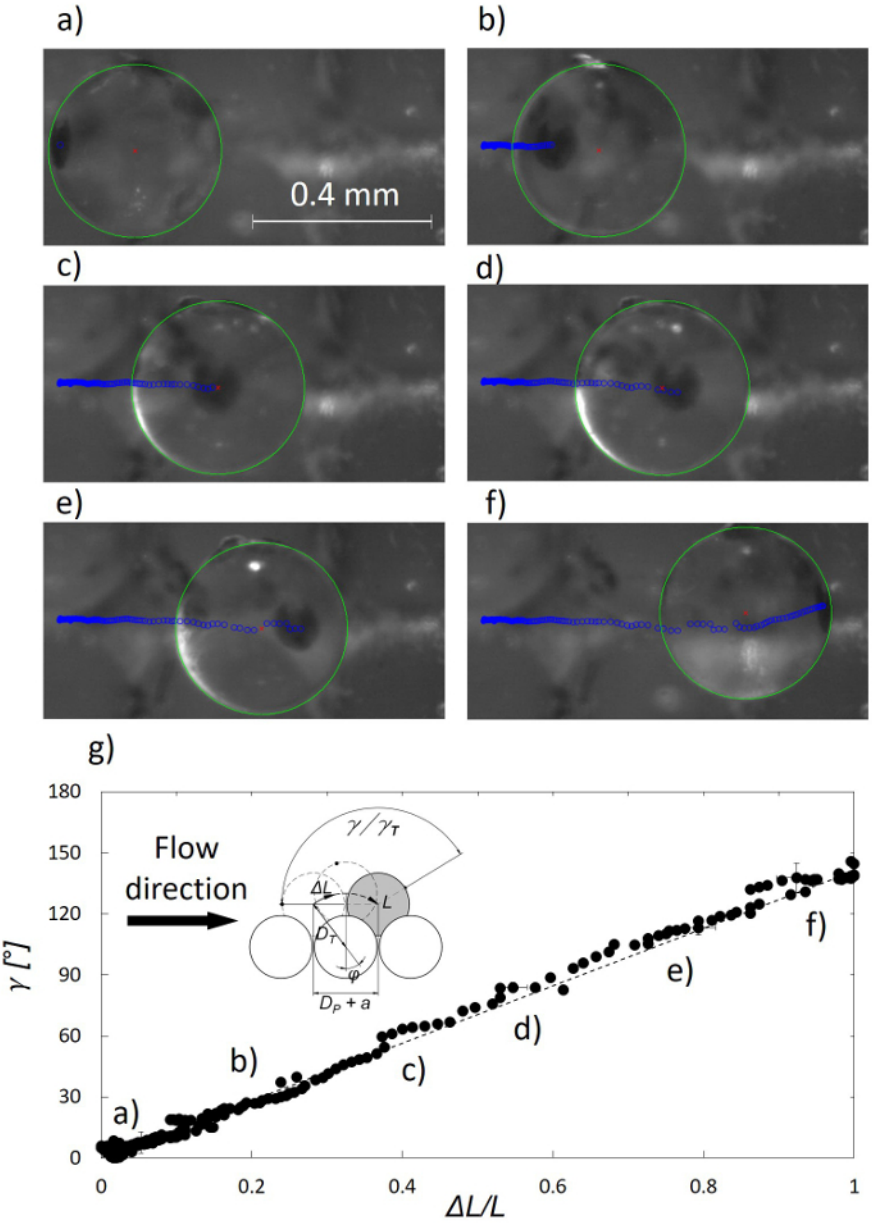

Figure 2: Snapshots during the incipient motion of a marked bead of (405.9 ± 8.7) µm diameter on the quadratic substrate with a spacing of 14 µm at Re* of approximately 0.06 (a)-(f). The red cross and the green line represent the center of the sphere, and the bead contour obtained from the algorithm, respectively. The blue circles represent the trajectory of the geometric center of the mark. Flow from left to right. The snapshots are reproduced from Agudo *et al (*2017)a[39], with the permission of AIP Publishing. Angle of rotation as a function of the curved trajectory along two equilibrium positions (g). The time instances of snapshots are indicated in the diagram. The dotted line indicates the angle of rotation for a pure rolling motion. **Figure 2(g)** is reproduced from Agudo *et al (*2014)[41], with the permission of AIP Publishing. Please click here to view a larger version of this figure.

Snapshots in **Figure 3(b) - (e)** depict an example for an alumina bead of (5 ± 0.25) mm displacing four positions over a quadratic substrate made of spheres of (2.00 ± 0.10) mm with no-gap between them. The video has been recorded from the side as in Section 2 (see steps 2.2.1-2.2.4). The measured angle agrees with the theoretical one during a path covering approximately the first two equilibrium position (see **Figure 3(g)**). Hence, rolling is assumed to be the mode of incipient motion and Eq. 8 can be used to calculate the critical Shields number. After the second equilibrium position, however, the measured rotation angle seems to deviate from pure rolling motion. The red line in **Figure 3(f)** represents the bead trajectory during a longer path of approximately 17 positions over the substrate. From the trajectory, it can be discerned how the particle experiences small flights during its motion along the substrate.

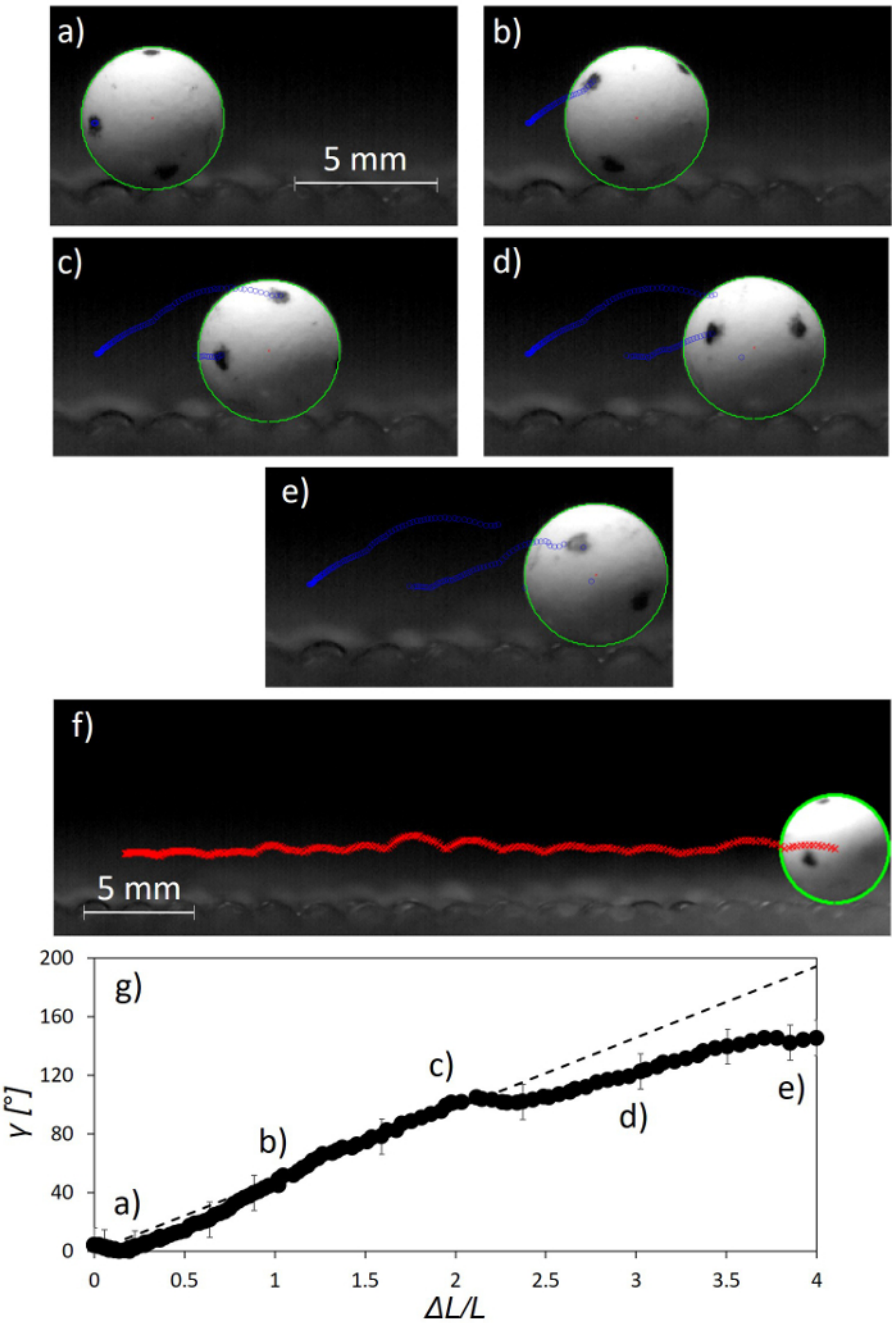

Figure 3: Snapshots during the incipient motion of a marked bead of (5.00 ± 0.25) mm diameter on the quadratic substrate with no spacing between spheres at Re* of approximately 87.5 (a) - (e). The red cross and the green line represent the center of the sphere, and the bead contour obtained from the algorithm, respectively. The blue circles represent the trajectory of the geometric center of the mark. The red crosses in (f) represent the trajectory of the bead center along approximately 17 positions along the substrate. Flow from left to right. Angle of rotation as a function of the curved trajectory along four equilibrium positions (g). The time instances of snapshots are indicated in the diagram. The dotted line indicates the angle of rotation for a pure rolling motion. Please click here to view a larger version of this figure.

Figure 4(a) illustrates the square-wave test to estimate the frequency response of the CTA at critical free-stream velocity for the alumina bead of (5 ± 0.25) mm (see step 2.3.5). The time required for the voltage to drop by 97%, T, is about 0.1 ms. Accordingly, the frequency response, given by $f_C = 1/1.3T$[60], results in approximately 7.7 kHz. From **Figure 4(a)**, it can be discerned that the undershoot remains well below the 15% of the peak response. This indicates that the hot-wire CTA parameters, including the overheating ratio, are properly tunned[61]. The calibration curves for the illustrative example are shown in **Figure 4(b)** before (red squares), and after the measurements of the velocity profile (black circles). Both curves overlap each other indicating that no changes occurred during the experiment. For the alumina bead of (5 ± 0.25) mm, the time-averaged velocity and the root square velocity are plotted as a function of the normalized wall-normal component in **Figure 4(c)** and **4(d)**, respectively. They are obtained as described in steps from 2.5.1 to 2.6.1 of the protocol. Both velocities are normalized with the critical free-stream velocity. From the maximum value in $u_{rms}/U_{\infty,C}$, it can be shown that the measured viscous sublayer thickness is approximately 0.25 mm. The solid line in **Figure 4(c)** represents a fit to the experimental data according to the logarithmic velocity law, Eq. 5, while the blue line represents a fit of the data according to the modified velocity law proposed by Rotta[20,58], Eq. 7. In this case, both fit are in good agreement since the viscous sublayer represents just a 5% of the mobile bead diameter. Accordingly, the shear velocity obtained from both fits differs by less than 8%. **Figure 4(e)** illustrates the action of fluctuating forces on the incipient motion from the energy criterion perspective as stated by Valyrakis *et al.* 2013[62]. The solid line shows a portion of the temporal history of the cube of instantaneous streamwise velocity, $u^3(t)$, measured at a distance of half the mobile alumina bead diameter from the substrate. The velocity was stored at a sampling rate of 25 kSa for this specific measurement. The blue line represents the cube of the averaged velocity, $\overline{u}^3$. The red dotted line represents the cube of the critical velocity calculated as in Valyrakis *et al.* 2011[63]

$$u_C = \sqrt{\frac{4}{3}\frac{\left(\frac{\rho_P}{\rho}-1\right)}{C_D E} f_H D_P g \tan\varphi} \qquad (10)$$

where f_H is the hydrodynamic mass coefficient, approximately equal to 1 in our experiments, and C_D is the drag coefficient assumed to be 0.9 as considered in Valyrakis *et al.* 2011[63]. $\tan\varphi$ and E are calculated as shown in Eq. 11 and 12, respectively. The instantaneous flow power is a linear function of the cube of velocity[62]. Therefore, peaks on $u^3(t)$ above the critical value may be considered as a potential trigger for incipient particle motion if the duration of those flow events last enough[62]. The self-developed algorithm estimates the duration of energetic flow events by evaluating the intersection of $u^3(t)$ with the horizontal line u_C^3 along the entire experiment. In the illustrative experiment depicted in **Figure 4**, the duration of energetic flow events is of the order of 1-2 ms with a maximum of 2.1 ms.

Copyright © 2018 Journal of Visualized Experiments

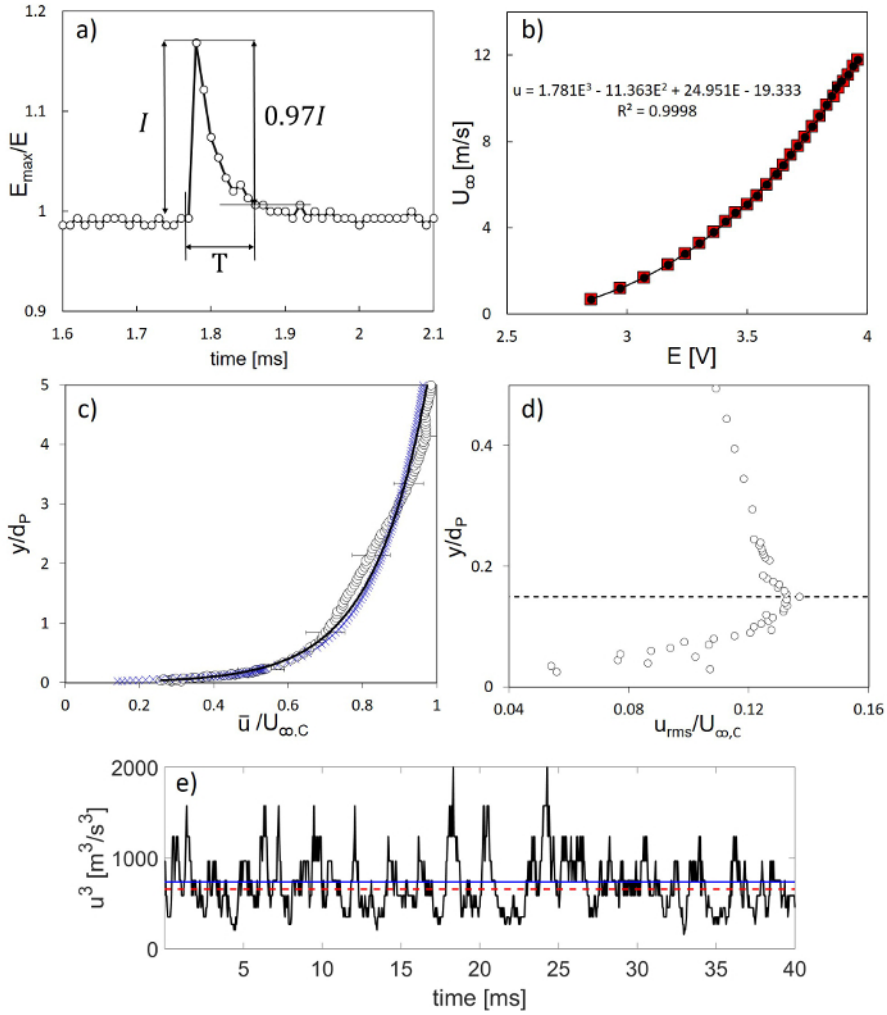

Figure 4: Representative results obtained with the hot wire CTA in the test section of the low-speed wind tunnel at onset of motion of the alumina bead of (5 ± 0.25) mm resting on a quadratic substrate with no spacing between spheres (a) Frequency response of the CTA after a square-wave test (b) Calibration curves before (red squares), and after the measurements of the velocity profile (black circles). The solid line indicates a third polynomial trend fit to the data. The fit coefficients are depicted in the inset of the figure (c) Time-averaged streamwise velocity profile. The solid line and blue symbols indicate a fit according to the logarithmic, and modified wall law, respectively (d) Root mean square streamwise velocity profile within a small height range. The measured viscous sublayer is about 0.25 mm (e) A portion of the temporal history of the cube of instantaneous streamwise velocity measured at a distance of half the mobile alumina bead diameter from the substrate. The blue line indicates the cube of the time-averaged streamwise velocity. The red dotted line indicates the cube of the critical velocity calculated as in Valyrakis *et al.* 2011[64]. Please click here to view a larger version of this figure.

Figure 5(a) represents the critical Shields number dependency as a function of the burial degree defined as Martino *et al.* 2009 by $\xi = \tan\varphi \,/\, E$[37]. The symbols marked in red are the threshold obtained from the illustrative examples in the protocol. The angle of repose and the exposure degree are geometrically coupled in our regular structures. The angle of repose can be analytically computed as follows:

$$\tan\varphi^{\Delta} = \frac{\frac{\sqrt{3}}{6}\frac{d_P}{D_P}}{\sqrt{\frac{1}{4}\left(1+\frac{d_P}{D_P}\right)^2 - \frac{1}{3}\left(\frac{d_P}{D_P}\right)^2}}, \qquad \tan\varphi^{\Pi} = \frac{1+\frac{a}{d_P}}{2\sqrt{\frac{1}{4}\left(1+\frac{D_P}{d_P}\right)^2 - \frac{1}{2}\left(1+\frac{a}{d_P}\right)^2}} \tag{11}$$

where the superscript Δ refers to the triangular geometry and $\prod$ refers to the quadratic geometry with spacing a between spheres. Similarly, the exposure degree defined as the cross-sectional area exposed to the flow yields:

$$E = 1 - \frac{\chi}{\pi} + \frac{\sin(2\chi)}{2\pi} \quad (12)$$

where χ is the angle the angle between the bead surface at effective zero level and the vertical axis (see inset of **Figure 5**). For the triangular and the quadratic substrate with spacing a between spheres, it can be shown that:

$$\cos\chi^{\Delta} = \frac{1+\frac{d_P}{D_P}}{\sqrt{1+4\tan^2\varphi^{\Delta}}} + 2\frac{z_0}{D_P} - \frac{d_P}{D_P}, \qquad \cos\chi^{\Pi} = \frac{1+\frac{d_P}{D_P}}{\sqrt{1+2\tan^2\varphi^{\Pi}}} + 2\frac{z_0}{D_P} - \frac{d_P}{D_P} \quad (13)$$

where z_0 is an effective zero level below the top of the substrate (see inset of **Figure 5**). In the creeping flow limit, numerical simulations show that the effective zero level increases linearly with the spacing a: $z_0/d_P = 0.077 + 0.13(a/d_P)$. At larger Re*, the effective zero level is assumed to be constant $z_0/d_P = 0.21$ as experimentally shown by Dey *et al.* 2012[64]. For Re* ranging between 40 and 150, the shear stress was inferred using the modified wall law that includes the hydraulically transitional flow regime. The solid and dotted line are power trends fitted to the experimental data. As shown in **Figure 5**, the critical Shields number increases as a function of the burial degree showing the strong influence of partially shielding the particle to the shear flow. This includes comparing triangular to quadratic substrate configurations and different mobile beads diameters. The influence of the sediment bed geometry seems to be more pronounced at higher Re*. For the same degree of protrusion, the critical Shields number at Re* below 1 remains well above the value at Re* ranging between 40 and 150.

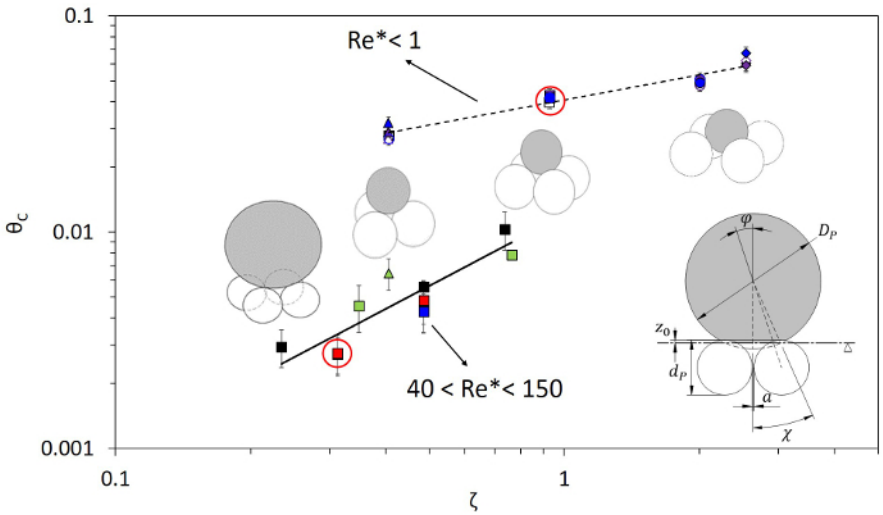

Figure 5: Dependence of the critical Shields number on the burial degree from laminar to turbulent flow conditions. At Re*<1, triangles, squares, circles and rhomboids indicate results obtained with triangular and quadratic substrates with a spacing of 14, 94 and 109 µm, respectively. Open and solid symbols represent experiments performed with less viscous and higher viscous oils, respectively. At 40<Re*<150, triangles and squares indicate experiments performed with triangular and quadratic substrates with no spacing, respectively. Black, blue, red, green and purple indicate experiments performed with glass, steel, alumina, polystyrene sulfonate, and Plexiglas, respectively. The data at Re*<1 are reproduced from Agudo *et al* (2012)[38], with the permission of AIP Publishing. Please click here to view a larger version of this figure.

Discussion

We present two different experimental methods for characterizing the incipient particle motion as a function of the sediment bed geometry. For that purpose, we use a monolayer of spheres regularly arranged according to a triangular or quadratic symmetry in such a way that the geometrical parameter simplifies to a single geometry. In the creeping flow limit, we describe the experimental method using a rotational rotameter to induce the laminar shear flow as in previous studies[39,40,41]. Preliminary experiments showed that the incipient motion remained independent of finite-size effects of the substrate such as the radial location, or the distance from the upstream border of the substrate[38]. Similarly, the critical Shields number was found to be independent of the relative flow submergence within an interval h/D_P ranging between 2 and 12 and independent of inertia up to a Re^* of about 3[38]. Above this value, an increase in the critical Shields number was observed as a consequence of interferences due to a secondary flow induced by the rotating plate. This factor limited the maximum Re^* for the experimental procedure described in the first part of the manuscript. The second experimental method is designed to address the hydraulically transitional and the rough turbulent flow regime. The shear stress is induced by a low-speed wind tunnel. In order to establish a range of parameters independent of any size or boundary effect of the substrate, we conducted measurements of the turbulent boundary layer at distances of 50, 80, 110, 140, 170 and 200 mm from the leading edge. At 50, 80, 110 and 200 mm, the boundary layer was measured at 4 different positions in the width direction, 55, 65, 95 and 125 mm from one of the substrate borders. At 140 and 170 mm, the boundary layer was measured at two different

positions in the width direction, 65 and 95 mm from one of the substrate border. All measurements were performed at critical free-stream velocity conditions, $U_{\infty,C}$ for a (5.00 ± 0.25) mm glass bead resting on a triangular substrate made of (2.00 ± 0.10) mm beads.Within the interval ranging between 80 and 200 mm, the shape factor ranged between 1.3 and 1.5 as expected for turbulent boundary layers[57]. The velocity profiles at the same distance from the leading edge were in good agreement with each other, revealing logarithmic coefficients that vary from 5% up to 10% independent of the width direction. The selected range of parameters in the description of the protocol is carefully chosen to ensure that the critical Shields number remained independent of any boundary effect of the experimental set-up. This holds true for both experimental methods.

The threshold for incipient motion depends on the mode of motion that in turn is a function of geometrical properties of the bed such as the exposure of the particle. At high Reynolds numbers, incipient motion is likely to happen by rolling if the particle is highly exposed to the flow[14,65]. For individual particles that are almost completely shielded by neighbors, however, lifting may be a more appropriate mode[14]. At laminar conditions, the situation simplifies since lift forces are usually neglected[16,17,40,44,45,66] and rolling or sliding is assumed to be the main mode for incipient motion. To properly characterize the critical Shields number as a function of the bed geometry, the mode of motion must first be thoroughly analyzed. For that purpose, we recorded the particle motion and we used an image process algorithms that calculates the angle of rotation of the bead[39]. If this value matches the theoretical angle for pure rolling as depicted in **Figure 2(g)** or in the initial range of **Figure 3(g)**, the critical Shields number can be inferred by using Eq. 1 and Eq. 8 for the Sections 1 and 2 of the protocol, respectively. The algorithm identifies particle positions and marks to study rotatory and sliding motion with a minimum of man interventions. The tracking of the particle is based on a Canny edge detector and Hough transform. This combination has been proven to provide a robust and reliable tool in studying granular transport processes[1,39,67,68]. On the other hand, the mark detection is based on simple gray-scale thresholding. The main disadvantage of the algorithm is that the threshold must be readjusted depending on the imaging system. Although the algorithm takes into account geometrical penalties s the marks, the tracking is more susceptible to errors caused by different threshold levels and light intensity fluctuations, as can be seen, for instance, from the blue circle indicating the centroid of a mark close to the bead center in the snapshot of **Figure 3(e)** and **3(f)**. For further applications, we propose to use cross-correlation techniques to detect mark displacements between subsequent frames. This may allow us to achieve a sub-pixel resolution[69] and may improve the detection of the angle when many marks are present.

Different definitions for the particle threshold are found in literature. At laminar conditions, as considered in Section 1, the critical Shields number as a dimensionless parameter for the onset of motion is usually defined as stated in Eq. 1, *i.e.* with the characteristic shear stress as $\tau = \mu\dot{\gamma}$[32,34,36,70]. Other dimensionless parameters as the Galileo number are also found in laminar flow[37]. This choice, however, might seem adequate at higher particle Reynolds numbers where inertia is more relevant than friction. The definition given in Eq. 1 seems to be particularly adequate in the creeping-flow limit where it has been shown that a deterministic modeling approach is valid when the geometrical parameter is simplified to a regular structure[40]. This statement is in agreement with maximum standard deviations of the order of 5-7% as measured with the experimental system described in Section 1. The standard deviation as estimated in the step 1.4.2.3, characterizes the random error associated with the rheometer and with fluctuations due to local imperfections on the substrate or in the bead size. Note that fluctuations in the hydrodynamic forces are not expected at Re* below one. Using the quadratic substrate with a spacing between beads of 14 µm, we obtained a critical Shields number equal to 0.040 ± 0.002[38]. The standard deviation was determined taking into account all individual measurements of **Figure 5**, *i.e.*, five different runs for each material combination in three different local positions. Values up to 7% for the standard deviation are found for other substrate configurations demonstrating the precision of the method. It is worth here to remark, that apart from deviations in the wire mesh size, the substrates sometimes present larger local imperfections such as cavities where the fixed bead has been detached or such as variations in height. A visual inspection of both top and side camera is therefore recommended before starting the measurement. High-resolution laser 3D printing may be used to build up the substrates in further applications where a sub-micron resolution is required.

When the bead is partially or fully exposed to the turbulent flow, as considered in Section 2, the role of peak turbulent-velocity values and its duration must be considered when we try to identify the incipient particle motion. The impulse[14,71] or the energy criterion[62] appear as a valuable alternative to the classical Shields criterion. They propose that apart from the hydrodynamic force, the characteristic time scale of flow structures must be properly parametrized[71]. For that purpose, the same algorithm that obtains time-averaged and root mean square velocities, estimates the duration of energetic flow events based on the condition $u(t) > u_C$. For the illustrative experiment of **Figure 4(e)**, the duration of energetic flow events remains of the order of 1-2 ms. If we used a drag coefficient given by $C_D = 0.55 + 37/\mathrm{Re}^{*1.2} - 3.5/\mathrm{Re}^{*0.9}$ in Eq. 10 as suggested by Vollmer and Kleinhans 2007[13] or Ali and Dey 2016[20] based on Coleman's experiments[72], the modified u_C remains above the previous value, and the measured maximum duration decreases to about 1.6 ms. In any case, the duration remains well below the order of 10 ms as observed in previous experiments of Valyrakis, Diplas *et al.* 2013 conducted in a water channel[62]. In addition, the algorithm determines the integral length scale as shown by El-Gabry, Thurman *et al.* 2014[73] based on Roach's method[74]. At a distance of half the bead diameter from the substrate, the estimated macro-scale length scale is about 1.5 mm. It has been shown that most of the energetic events able to trigger the incipient motion should have a characteristic length of about two to four particle diameters[62]. This statement may thus indicate that the energetic events induced in our low-speed wind tunnel are not able to trigger the incipient motion. This is in agreement with an averaged velocity slightly above the critical value as shown in **Figure 4(e)**, and with standard deviations below 8% in $U_{\infty,C}$ for 5 mm beads independent of the material as noticed in the experiments. The standard deviation in $U_{\infty,C}$ as calculated in steps 2.2.5-2.2.6 provides an estimation of the random fluctuation associated with the flow parameters but also to local imperfections on the regular substrate. For the alumina bead of 5 mm diameter, we obtained an $U_{\infty,C}$ equal to 12.30 ± 0.23 m/s. This standard deviation was determined taking into account 10 individual runs in three different positions at the same distance from the leading edge. For beads of 2 mm, the standard deviation increases up to approximately 14%. In view of this results, we decided to use the Shields criterion with a critical Shields number as defined in Eq. 8 to characterize the incipient motion. In addition, instead of presenting a probability of entrainment, we opt to provide a specific value of the critical Shields number with a representative degree of uncertainty. There are two main

sources of uncertainty in Eq. 6 in order to evaluate the shear velocity: $U_{\infty,C}$ and b. The relative uncertainty on $U_{\infty,C}$ is inferred from the standard deviation of the measurements. The relative uncertainty in b is related to the measurement of the turbulent boundary layer. At the same distance from the leading edge, typical deviations on the fit coefficient range between 5 and 10% depending on the fan speed that in turns depends on the substrate geometry and the bead density. The relative uncertainty in b was assumed to be 10% in the most conservative analysis. Accordingly, the uncertainty of u^* ranges between 7 and 18% depending on the experiment. Error bars in **Figure 5** display the uncertainty of the Shields number after applying the aforementioned analysis including relative uncertainties on the particle diameter, and air and particle densities.

The experimental protocol allows the characterization of the incipient particle motion as a function of the burial degree in different flow regimes. The use of regular geometries simplifies the geometrical factor to a single geometry and avoids any doubt about the role of the neighborhood. The criterion for incipient motion is satisfied when the bead moves from its initial position to the next equilibrium one. The use of an image processing algorithm clarifies the mode of incipient motion. The experimental method described in Section 1 of the protocol has been used in previous studies to point out the strong impact of the local bed arrangement on the incipient motion under laminar conditions[38,39,40,41]. The system, however, was limited to Re* below 3. At higher Re*, we propose a new experimental method that permits us to address the hydraulically transitional and the rough turbulent flow regime. Interestingly, the turbulence characteristics of the system in conjunction with a simplified geometrical parameter allows us to characterize the incipient motion with a critical Shields number with uncertainties that ranges between 14 and 25%. We present just some representative examples of the application at Re* ranging between 40 and 150. As a future scope of the research study, a broader range of the Re* must be covered with special emphasis on the hydraulically transitional flow regime where fewer data are available in literature. Similarly, experiments at larger burial degrees should be conducted. These results may be used as a benchmark for more complex models. For example, the realistic model recently proposed by Ali and Dey 2016 is based on a hindrance coefficient that is inferred from experimental results only for the case of closely packed sediment beads[20]. Experimental results for particles that are less exposed to the flow as addressed in the creeping flow limit may trigger an extrapolation of the model at larger burial degrees. In addition, the proposed experimental method may permit us to emphasize on the role of turbulent coherent structures on the incipient particle motion with a strong simplification of the geometrical factor. This is still poorly understood in literature.

Disclosures

The authors have nothing to disclose

Acknowledgements

The authors are thankful to unknown referees for valuable advice and to Sukyung Choi, Byeongwoo Ko and Baekkyoung Shin for the collaboration in setting up the experiments. This work was supported by the Brain Busan 21 Project in 2017.

References

1. Groh, C., Wierschem, A., Aksel, N., Rehberg, I., & Kruelle, C. A. Barchan dunes in two dimensions: Experimental tests for minimal models. *Phys. Rev. E.* **78**, 021304 (2008).
2. Wierschem, A., Groh, C., Rehberg, I., Aksel, N., & Kruelle, C. Ripple formation in weakly turbulent flow. *Eur. Phys. J. E.* **25**, 213-221 (2008).
3. Herrmann, H. *Dune Formation in Traffic and Granular Flow.* Springer, Berlin (2007).
4. Stevanovic, V. D. *et al.* Analysis of transient ash pneumatic conveying over long distance and prediction of transport capacity. *Powder Technol.* **254**, 281-290 (2014).
5. Fan, F.-G., Soltani, M., Ahmadi, G., & Hart, S. C. Flow-induced resuspension of rigid-link fibers from surfaces. *Aerosol. Sci. Tech.* **27**, 97-115 (1997).
6. Burdick, G., Berman, N., & Beaudoin, S. Hydrodynamic particle removal from surfaces. *Thin Solid Films.* **488**, 116-123 (2005).
7. Chang, Y. Laboratory investigation of flume traction and transportation in *Proceedings of the American Society of Civil Engineers.* 1701-1740 (1939).
8. Paintal, A. A stochastic model of bed load transport. *J. Hydraul. Res.* **9**, 527-554 (1971).
9. Mantz, P. A. Incipient transport of fine grains and flakes by fluids-extended shield diagram. *J. Hydr. Eng. Div.-Asce.* **103** (1977).
10. Yalin, M. S., & Karahan, E. Inception of sediment transport. *J. Hydr. Eng. Div.-Asce.* **105**, 1433-1443 (1979).
11. Kuhnle, R. A. Incipient motion of sand-gravel sediment mixtures. *J. Hydraul. Eng.* **119**, 1400-1415 (1993).
12. Marsh, N. A., Western, A. W., & Grayson, R. B. Comparison of methods for predicting incipient motion for sand beds. *J. Hydraul. Eng.* **130**, 616-621 (2004).
13. Vollmer, S., & Kleinhans, M. G. Predicting incipient motion, including the effect of turbulent pressure fluctuations in the bed. *Water Resour. Res.* **43** (2007).
14. Valyrakis, M., Diplas, P., Dancey, C. L., Greer, K., & Celik, A. O. Role of instantaneous force magnitude and duration on particle entrainment. *J. Geophys. Res.-Earth.* **115** (2010).
15. Dey, S., & Ali, S. Z. Stochastic mechanics of loose boundary particle transport in turbulent flow. *Phys. Fluids.* **29**, 055103 (2017).
16. Wiberg, P. L., & Smith, J. D. Calculations of the critical shear stress for motion of uniform and heterogeneous sediments. *Water Resour. Res.* **23**, 1471-1480 (1987).
17. Ling, C.-H. Criteria for incipient motion of spherical sediment particles. *J. Hydraul. Eng.* **121**, 472-478 (1995).
18. Dey, S. Sediment threshold. *Appl. Math. Model.* **23**, 399-417 (1999).
19. Bravo, R., Ortiz, P., & Pérez-Aparicio, J. Incipient sediment transport for non-cohesive landforms by the discrete element method (DEM). *Appl. Math. Model.* **38**, 1326-1337 (2014).

Copyright © 2018 Journal of Visualized Experiments

20. Ali, S. Z., & Dey, S. Hydrodynamics of sediment threshold. *Phys. Fluids.* **28**, 075103 (2016).
21. Yalin, M. S. *Mechanics of sediment transport.* Pergamon Press. California (1977).
22. Graf, W. H., & Sueska, L. Sediment transport in steep channels. *Journal of Hydroscience and Hydraulic Engineering.* **5**, 233-255 (1987).
23. Recking, A. *An experimental study of grain sorting effects on bedload.* Doctor in Sciences thesis, Institut National des Sciences Appliques de Lyon. Lyon (2006).
24. Roušar, L., Zachoval, Z., & Julien, P. Incipient motion of coarse uniform gravel. *J. Hydraul. Res.* **54**, 615-630 (2016).
25. Miller, R. L., & Byrne, R. J. The angle of repose for a single grain on a fixed rough bed. *Sedimentology.* **6**, 303-314 (1966).
26. Fenton, J., & Abbott, J. Initial movement of grains on a stream bed: the effect of relative protrusion in *Proceedings of the Royal Society of London A: Mathematical, Physical and Engineering Sciences.* **352**, 523-537 (1977).
27. Kirchner, J. W., Dietrich, W. E., Iseya, F., & Ikeda, H. The variability of critical shear stress, friction angle, and grain protrusion in water-worked sediments. *Sedimentology.* **37**, 647-672 (1990).
28. Armanini, A., & Gregoretti, C. Incipient sediment motion at high slopes in uniform flow condition. *Water Resour. Res.* **41** (2005).
29. Chin, C., & Chiew, Y. Effect of bed surface structure on spherical particle stability. *J. Waterw. Port Coast.* **119**, 231-242 (1993).
30. Whitehouse, R., & Hardisty, J. Experimental assessment of two theories for the effect of bedslope on the threshold of bedload transport. *Mar. Geol.* **79**, 135-139 (1988).
31. Buffington, J. M., & Montgomery, D. R. A systematic analysis of eight decades of incipient motion studies, with special reference to gravel-bedded rivers. *Water Resour. Res.* **33**, 1993-2029 (1997).
32. Charru, F., Mouilleron, H., & Eiff, O. Erosion and deposition of particles on a bed sheared by a viscous flow. *J. Fluid Mech.* **519**, 55-80 (2004).
33. Loiseleux, T., Gondret, P., Rabaud, M., & Doppler, D. Onset of erosion and avalanche for an inclined granular bed sheared by a continuous laminar flow. *Phys. Fluids.* **17**, 103304 (2005).
34. Charru, F., Larrieu, E., Dupont, J.-B., & Zenit, R. Motion of a particle near a rough wall in a viscous shear flow. *J. Fluid Mech.* **570**, 431-453 (2007).
35. Ouriemi, M., Aussillous, P., Medale, M., Peysson, Y., & Guazzelli, É. Determination of the critical Shields number for particle erosion in laminar flow. *Phys. Fluids.* **19**, 061706 (2007).
36. Lobkovsky, A. E., Orpe, A. V., Molloy, R., Kudrolli, A., & Rothman, D. H. Erosion of a granular bed driven by laminar fluid flow. *J. Fluid Mech.* **605**, 47-58 (2008).
37. Martino, R., Paterson, A., & Piva, M. Onset of motion of a partly hidden cylinder in a laminar shear flow. *Phys. Rev. E.* **79**, 036315 (2009).
38. Agudo, J., & Wierschem, A. Incipient motion of a single particle on regular substrates in laminar shear flow. *Phys. Fluids.* **24**, 093302 (2012).
39. Agudo, J. *et al.* Detection of particle motion using image processing with particular emphasis on rolling motion. *Rev. Sci. Instrum.* **88**, 051805 (2017).
40. Agudo, J. *et al.* Shear-induced incipient motion of a single sphere on uniform substrates at low particle Reynolds numbers. *J. Fluid Mech.* **825**, 284-314 (2017).
41. Agudo, J., Dasilva, S., & Wierschem, A. How do neighbors affect incipient particle motion in laminar shear flow? *Phys. Fluids.* **26**, 053303 (2014).
42. Seizilles, G., Lajeunesse, E., Devauchelle, O., & Bak, M. Cross-stream diffusion in bedload transport. *Phys. Fluids.* **26**, 013302 (2014).
43. Seizilles, G., Devauchelle, O., Lajeunesse, E., & Métivier, F. Width of laminar laboratory rivers. *Phys. Rev. E.* **87**, 052204 (2013).
44. Hong, A., Tao, M., & Kudrolli, A. Onset of erosion of a granular bed in a channel driven by fluid flow. *Phys. Fluids.* **27**, 013301 (2015).
45. Derksen, J., & Larsen, R. Drag and lift forces on random assemblies of wall-attached spheres in low-Reynolds-number shear flow. *J. Fluid Mech.* **673**, 548-573 (2011).
46. Happel, J., & Brenner, H. *Low Reynolds Number Hydrodynamics: With Special Applications to Particulate Media*. Martinuis Nijhoff. The Hague (1983).
47. Lajeunesse, E. *et al.* Fluvial and submarine morphodynamics of laminar and near-laminar flows: A synthesis. *Sedimentology.* **57**, 1-26 (2010).
48. Aussillous, P., Chauchat, J., Pailha, M., Médale, M., & Guazzelli, É. Investigation of the mobile granular layer in bedload transport by laminar shearing flows. *J. Fluid Mech.* **736**, 594-615 (2013).
49. Thompson, J. A., & Bau, H. H. Microfluidic, bead-based assay: Theory and experiments. *J. Chromatogr. B.* **878**, 228-236 (2010).
50. Sawetzki, T., Rahmouni, S., Bechinger, C., & Marr, D. W. In situ assembly of linked geometrically coupled microdevices. *Proceedings of the National Academy of Sciences.* **105**, 20141-20145 (2008).
51. Amini, H., Sollier, E., Weaver, W. M., & Di Carlo, D. Intrinsic particle-induced lateral transport in microchannels. *Proceedings of the National Academy of Sciences.* **109**, 11593-11598 (2012).
52. Soepyan, F. B. *et al.* Threshold velocity to initiate particle motion in horizontal and near-horizontal conduits. *Powder Technol.* **292**, 272-289 (2016).
53. Deskos, G., & Diplas, P. Incipient motion of a non-cohesive particle under Stokes flow conditions. *International Journal of Multiphase Flow.* (2017).
54. Julien, P. Y. *Erosion and sedimentation.* Cambridge University Press, Cambridge (2010).
55. Jimenez, J. Turbulent flows over rough walls. *Annu. Rev. Fluid Mech.* **36**, 173-196 (2004).
56. O'neill, P., Nicolaides, D., Honnery, D., & Soria, J. in *15th Australasian Fluid Mechanics Conference.* 1-4 (The University of Sydney) (2006).
57. Schlichting, H. *Boundary-Layer Theory.* McGraw-Hill. New York (1979).
58. Rotta, J. Das in wandnähe gültige Geschwindigkeitsgesetz turbulenter Strömungen. *Arch. Appl. Mech.* **18**, 277-280 (1950).
59. Schlichting, H., Gersten, K., Krause, E., & Oertel, H. *Boundary-layer theory.* Vol. 7, Springer, (1955).
60. Bruun, H. H. *Hot-wire anemometry-principles and signal analysis.* Oxford: University Express. Oxford (1995).
61. Fan, D., Cheng, X., Wong, C. W., & Li, J.-D. Optimization and Determination of the Frequency Response of Constant-Temperature Hot-Wire Anemometers. *AIAA J.*, 1-7 (2017).
62. Valyrakis, M., Diplas, P., & Dancey, C. L. Entrainment of coarse particles in turbulent flows: An energy approach. *J. Geophys. Res.-Earth.* **118**, 42-53 (2013).
63. Valyrakis, M., Diplas, P., & Dancey, C. L. Entrainment of coarse grains in turbulent flows: An extreme value theory approach. *Water Resour. Res.* **47** (2011).
64. Dey, S., Das, R., Gaudio, R., & Bose, S. Turbulence in mobile-bed streams. *Acta Geophys.* **60**, 1547-1588 (2012).
65. Wu, F.-C., & Chou, Y.-J. Rolling and lifting probabilities for sediment entrainment. *J. Hydraul. Res.* **129**, 110-119 (2003).
66. Leighton, D., & Acrivos, A. The lift on a small sphere touching a plane in the presence of a simple shear flow. *Z. Angew. Math. Phys.* **36**, 174-178 (1985).

Copyright © 2018 Journal of Visualized Experiments

67. Tuyen, N. B., & Cheng, N.-S. A single-camera technique for simultaneous measurement of large solid particles transported in rapid shallow channel flows. *Exp. Fluids.* **53**, 1269-1287 (2012).
68. Gollin, D., Bowman, E., & Shepley, P. Methods for the physical measurement of collisional particle flows. *IOP Conference Series: Earth and Environmental Science.* **26**, 012017 (2015).
69. Amon, A. *et al.* Focus on Imaging Methods in Granular Physics. *Rev. Sci. Instrum.* **88** (2017).
70. Mouilleron, H., Charru, F., & Eiff, O. Inside the moving layer of a sheared granular bed. *J. Fluid Mech.* **628**, 229-239 (2009).
71. Diplas, P. *et al.* The role of impulse on the initiation of particle movement under turbulent flow conditions. *Science.* **322**, 717-720 (2008).
72. Coleman, N. L. A theoretical and experimental study of drag and lift forces acting on a sphere resting on a hypothetical streambed. *International Association for Hydraulic Research, 12th Congress, proceedings.*, **3**, 185-192 (1967).
73. El-Gabry, L. A., Thurman, D. R., & Poinsatte, P. E. *Procedure for determining turbulence length scales using hotwire anemometry.* NASA Technical Reports NASA/TM-2014-218403 (2014).
74. Roach, P. The generation of nearly isotropic turbulence by means of grids. *Int. J. Heat Fluid Fl.* **8**, 82-92 (1987).

Copyright © 2018 Journal of Visualized Experiments